Computers and Fluids 140 (2016) 72–80

Contents lists available at ScienceDirect

Computers and Fluids

journal homepage: www.elsevier.com/locate/compfluid

Bifurcation analysis of laminar isothermal planar opposed-jet flow

Shuang Liu [a], Bofu Wang [b], Zhenhua Wan [a,*], Dongjun Ma [c], Dejun Sun [a]

[a] Department of Modern Mechanics, University of Science and Technology of China, Hefei 230027, Anhui, China
[b] Shanghai Institute of Applied Mathematics and Mechanics, and Shanghai Key Laboratory of Mechanics in Energy Engineering, Shanghai University, Shanghai 200072, China
[c] Institute of Applied Physics and Computational Mathematics, Beijing 100088, China

ARTICLE INFO

Article history:
Received 11 September 2015
Revised 11 May 2016
Accepted 8 September 2016
Available online 9 September 2016

MSC:
00-01
99-00

Keywords:
Hydrodynamic instability
Bifurcation
Opposed-jet flow
Model equations
Symmetry

ABSTRACT

For a fixed geometric configuration, hydrodynamic instabilities and bifurcation processes of laminar isothermal planar opposed-jet flows with symmetric and slightly asymmetric inlet boundary conditions are investigated numerically using a high-resolution approach based on spectral element method. In current configuration, when inlet boundary conditions are symmetric, in the range of the Reynolds number considered ($Re \leq 200$), multiple new symmetry-breaking bifurcations are observed and four new flow patterns are identified. Their hydrodynamic characteristics are analyzed, in particular their symmetries. In addition, the case that inlet boundary conditions are slightly asymmetric is investigated. It is found that bifurcation processes are extremely sensitive to this small symmetry-breaking imperfection and much different from those in the symmetric case. Furthermore, model equations are constructed by symmetry consideration to explain the numerical results based on hydrodynamic equations.

1. Introduction

Opposed-jet flows can greatly enhance fluid mixing efficiency and have been applied in a variety of industrial applications such as polymer processing [1] and nanoparticle synthesis [2]. A comprehensive discussion on opposed-jet reactor applications can be found in Refs. [3,4]. Knowledge about various flow instabilities and bifurcation processes are important for setting appropriate working conditions for opposed-jet flows. Besides the practical importance, the opposed-jet flow system is one of many nonlinear hydrodynamic systems exhibiting complex and fascinating dynamics, the investigation of which is of great theoretical significance. Relevant studies have been carried out by many researchers through experimental, numerical or theoretical methods for non-isothermal and isothermal opposed-jet flows.

The non-isothermal opposed-jet flows taking into account thermal instabilities have been investigated extensively, especially in combustion community. The major research effort has focused on the determination of ignition and extinction conditions of the diffusion flames [5,6]. Without considering thermal instabilities, many researchers have studied the hydrodynamic instabilities of isothermal symmetric opposed-jet flows. Rolon et al. [7] investigated isothermal opposed-jet flows of air experimentally using contoured nozzles to produce uniform velocity profiles. When the inlet mass flow rates were identical, they observed that besides the symmetric flow pattern, there existed two stable and steady flow states with broken symmetry, in which the stagnation point deviated from the center toward one or the other inlet. These two asymmetric flow states were mirror images of each other. Denshchikov et al. [8,9] investigated isothermal opposed-jet flows of water experimentally, and they observed periodically oscillating flow pattern under certain flow rates and geometric configurations, in which two jets were deflected in the opposite directions which were periodically switched. Pawlowski et al. [10] carried out a numerical study of the structure and stability of laminar isothermal opposed-jet flows with uniform velocity profiles of identical amplitude in planar and axisymmetric geometries. In the planar geometry with various aspect ratios, four flow regimes were found, which were symmetric steady regime, multiple steady regime, deflecting jet regime and time-dependent chaotic regime with vortex shedding, respectively. Using numerical bifurcation analysis and linear stability analysis, they revealed the transitions between a single (symmetric) steady state and multiple steady states or periodic steady states. In the axisymmetric geometry, only symmetric steady and multiple steady regimes were identified.

* Corresponding author.
E-mail address: wanzh@ustc.edu.cn (Z. Wan).

http://dx.doi.org/10.1016/j.compfluid.2016.09.007
0045-7930/

There are also some studies considering how the asymmetry of inlet boundary conditions affects opposed-jet flows. For instance, Ciani et al. [11] performed experimental and numerical studies on opposed-jet flow with non-uniform velocity profiles in axisymmetric configuration. They found experimentally that, when inflow velocities were identical and amplitudes were small, flow fields were symmetric. Moreover, as velocity amplitude increased, asymmetric flow fields were identified. Corresponding bifurcation diagram was obtained by means of numerical bifurcation analysis. When the velocity of one jet (the corresponding Reynolds number was denoted by Re_1) was fixed with a small amplitude, the stagnation plane location (*SPL*) was found experimentally to change smoothly with the variation of Re_2 (the Reynolds number corresponding to the other jet). When Re_1 was large enough, a hysteretic jump of *SPL* could be observed as Re_2 varied.

Instabilities in a related class of cross-slot flow have also been studied [12–14]. Arratia et al. [12] studied the flow of dilute polymer solutions in a cross-slot microchannel. As the Deborah number was increased, they identified a transition to steady asymmetric flow which was invariant to a spatial rotation of angle π around the center. A second transition to time-dependent flow occured at higher Deborah number. Motivated by these experimental observations, Poole et al. [13] performed numerical simulations on two-dimensional cross-slot flow of a viscoelastic fluid described by the upper-convected Maxwell model under low Reynolds number flow conditions and observed qualitatively similar flow behaviors. It was demonstrated that the transition to steady asymmetric state originated from elastic instability. Poole et al. [14] studied inertial instability of cross-slot flow of a Newtonian fluid. They found that, as Reynolds number was increased, steady asymmetric flow appeared after a supercritical pitchfork bifurcation. This asymmetric flow is different from that observed for inertialess viscoelastic fluid flow [13] and invariant to a spatial reflection about the mid-plane halfway between the two outlets.

Bifurcations and control of flow in a similar configuration with three inlets and one outlet (the X-junction flow) were studied by Lashgari et al. [15] via linear stability analysis and direct numerical simulations. As *Re* increased, a symmetry-breaking pitchfork bifurcation occurred due to a lift-up mechanism and the flow became asymmetric. Distributed suction or blowing at the walls computed through a sensitivity analysis was used for instability control and shown to delay this bifurcation significantly. At higher *Re*, flow became three dimensional through a secondary bifurcation.

In this paper we aim to investigate hydrodynamic instabilities and bifurcation processes of opposed-jet flow using numerical bifurcation analysis. For a fixed configuration in Ref. [10], instabilities and bifurcations are studied in a broad range of *Re*. When inlet boundary conditions are symmetric, multiple new symmetry-breaking bifurcations are observed and four new flow patterns are found. Considering that the presence of symmetry of opposed-jet flow system is the result of an idealization and symmetry plays an important role in the bifurcation process [16–18], we investigate the case that inflow velocities are slightly different. The results demonstrate that this small symmetry-breaking imperfection has a great influence on the bifurcation processes of opposed-jet flow. Moreover, model equations are constructed by symmetry consideration and used to explain the numerical results based on hydrodynamic equations qualitatively.

The rest of the paper is organized as follows. Section 2 describes the problem and flow configuration. Then we describe the essentials of numerical approaches and make validation for our numerical solvers in Section 3. Detailed results are presented and discussions are made in Section 4. Finally, some remarks and conclusions are drawn.

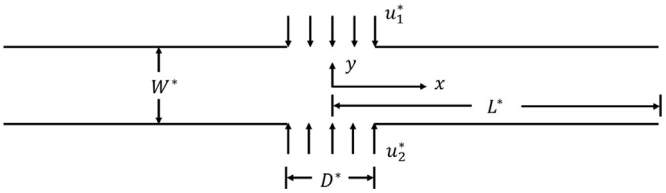

Fig. 1. Schematic of opposed-jet flow system.

2. Problem description

The schematic of planar opposed-jet flow system in the Cartesian coordinate is illustrated in Fig. 1. The variables D^*, W^* and L^* (the superscript indicates dimensional quantities) are the width of the inlet, the spacing between two inlets and the distance between the outlet and the mid-plane $x = 0$, respectively. Flow region is confined by two parallel horizontal walls at $y = \pm W^*/2$. It is noted that the opposed-jet flow model under investigation is two-dimensional and the flow is assumed to be homogenous in the third dimension even at the highest Reynolds number considered.

The Navier–Stokes equations are employed to describe the behavior of isothermal incompressible Newtonian fluid flow. The governing equations are expressed below in dimensionless form

$$\begin{aligned} &\nabla \cdot \vec{u} = 0, \\ &\frac{\partial \vec{u}}{\partial t} + \vec{u} \cdot \nabla \vec{u} = -\nabla p + \frac{1}{Re} \nabla^2 \vec{u}, \end{aligned} \tag{1}$$

where $\vec{u} = (u, v)$ is the velocity vector and p is the pressure. Length, velocity, time and pressure are scaled by D^*, u_2^*, D^*/u_2^*, and $\rho^* u_2^{*2}$, respectively, where ρ^* is the fluid density. Reynolds number is defined as $Re = \rho^* D^* u_2^*/\eta^*$, where η^* denotes the dynamical viscosity of the fluid. A dimensionless parameter $\theta = (u_1^* - u_2^*)/u_2^*$ is introduced to measure the difference between inlet velocities. Moreover, there is a geometric parameter defined as $\alpha = D^*/W^*$.

The above set of equations is supplemented with the following boundary conditions. Uniform velocity profiles which can be produced in contoured nozzles experimentally are prescribed at the upper and lower inlets, whose amplitudes are u_1^* and u_2^*, respectively. The no-slip and no-penetration boundary conditions are prescribed at the solid walls. It is supposed that the flow near the outlet is well developed.

In this study, the geometric parameter α is fixed at 0.25. The opposed-jet flow bifurcation is investigated for $\theta = 0$ and $\theta = 0.01$ with *Re* up to 200. The horizontal length L^* is set to be $10W^*$ which is large enough to ensure that the outlet boundary condition does not affect the flow structure in the stagnation region and the bifurcation results throughout the *Re* range we have considered.

When $\theta = 0$, the governing equations and boundary conditions are equivariant to a spatial reflection K_x about the mid-plane $x = 0$ and a rotation R_π of angle π around the center. Thus, the symmetry group of the problem is D_2 [17]. Its action on the velocity vector $\vec{u}$ is

$$\begin{aligned} K_x(u, v)(x, y) &= (-u, v)(-x, y), \\ R_\pi(u, v)(x, y) &= (-u, -v)(-x, -y). \end{aligned} \tag{2}$$

When $\theta \neq 0$, the up-down symmetry of the problem is broken and the governing equations and boundary conditions are equivariant to only the spatial reflection K_x about mid-plane $x = 0$. Thus, the symmetry group of the problem is Z_2.

3. Numerical approaches and validation

3.1. Numerical approaches

In this study opposed-jet flow system is analyzed through computation of transient and steady solutions and linear stability analysis of steady flows. The numerical approaches are described in the following sections.

3.1.1. Transient-state solver

The domain decomposition Stokes algorithm [19] is utilized to solve the governing Eq. (1) using a spectral/*hp* element solver [20]. The computation domain is decomposed into non-overlapping spectral elements $\{\Omega_j\}$. The unknowns are approximated by high-order Gauss–Legendre–Lobatto polynomials in each element Ω_j. The discrete equations are obtained from the following variational weak form of the governing equations

$$(\partial_t \vec{u}, \vec{\omega}) + \frac{1}{Re}(\nabla \vec{u}, \nabla \vec{\omega}) + (\vec{u} \cdot \nabla \vec{u}, \vec{\omega}) - (p, \nabla \cdot \vec{\omega}) = 0,$$
$$(\nabla \cdot \vec{u}, q) = 0, \qquad (3)$$

where $\vec{\omega}$ and q are trial functions and $(\cdot, \cdot)$ is the inner product defined as $(\phi, \psi) = \int_{\Omega_j} \phi(x)\psi(x)dx$.

The second-order stiff stable scheme [21] is adopted for time integration. The linear terms are treated implicitly and the nonlinear terms explicitly. Then the discretized variational weak form is re-formed with an unsteady Stokes operator on the left-hand side and explicit forcing terms on the right-hand side. In the domain decomposition approach, the interior and marginal degrees of freedom are decoupled and the divergence-free condition is satisfied strictly. The resulting linear system in each element is solved by direct method.

3.1.2. Steady-state solver

The Navier–Stokes equations can be re-formed as

$$\begin{aligned}\partial_t \vec{u} &= -\nabla p - \vec{u} \cdot \nabla \vec{u} + \frac{1}{Re}\nabla^2 \vec{u} \\ &= -(I - \nabla \nabla^{-2} \nabla \cdot)(\vec{u} \cdot \nabla \vec{u}) + \frac{1}{Re}\nabla^2 \vec{u} \\ &= N(\vec{u}) + L\vec{u}, \end{aligned} \qquad (4)$$

where N and L represent the nonlinear and linear operators, respectively. For first-order implicit/explicit Euler scheme we have

$$\frac{\vec{u}^{n+1} - \vec{u}^n}{\Delta t} = N(\vec{u}^n) + L\vec{u}^{n+1} = (I - \Delta t L)^{-1}(N + L)\vec{u}^n. \qquad (5)$$

The steady Navier–Stokes equations read

$$0 = N(\vec{u}) + L\vec{u}. \qquad (6)$$

Applying Newton's method to Eq. (6), in each iteration the approximate solution $\vec{u}$ to Eq. (6) is updated by a correction $\delta\vec{u}$ which satisfies the following linear equation

$$(N_{\vec{u}} + L)\delta\vec{u} = -(N + L)\vec{u}, \qquad (7)$$

where $N_{\vec{u}}$ is the Jocabian matrix associated with the nonlinear term N evaluated at state $\vec{u}$. A Jacobian-free Newton-Krylov method [22] is used to obtain stable or unstable steady solutions. Unsteady Stokes algorithm is used as the preconditioner of the Newton iteration [23]. Using $(I - \Delta t L)^{-1}\Delta t$ as a preconditioner, the linear system for Newton iteration can be reformulated as

$$(I - \Delta t L)^{-1}\Delta t\left(N_{\vec{u}} + L\right)\delta\vec{u} = -(I - \Delta t L)^{-1}\Delta t(N + L)\vec{u}. \qquad (8)$$

Inexact Newton method is used for accelerating convergence [24,25]. The right- and left-hand side of Eq. (8) are calculated by time-stepping methods based on Eq. (5). The nonlinear iterative process is terminated when the relative residual is less than 10^{-12}.

Table 1
The critical Reynolds number Re_{cr} of the first primary bifurcation of opposed-jet flow with $\theta = 0$ using different meshes and orders of interpolating polynomials n.

Spectral elements	n	$\sigma(Re = 45)$	$\sigma(Re = 47)$	Re_{cr}
4834	4	−1.477E−3	1.020E−3	46.2
7888	4	−1.287E−3	1.203E−3	46.0
7888	5	−1.286E−3	1.230E−3	46.0
11,222	4	−1.286E−3	1.231E−3	46.0

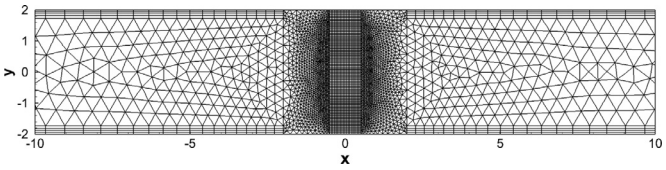

Fig. 2. Spectral element distribution at the central region of mesh comprising 7888 elements.

Steady-state solution branch is tracked by using Newton's method as a function of a continuation parameter which is *Re* in this study. Once a steady solution is obtained by using direct numerical simulation or Newton iteration with a specific initial condition, using it as the initial guess, solutions at adjacent *Re* can be obtained by Newton iteration. In this way, as *Re* varies, the whole solution branch can be obtained.

3.1.3. Linear stability analysis

The evolution of infinitesimal perturbations $\vec{u}'$ from a steady base flow $\vec{u}$ is governed by the following linearized Navier–Stokes equation

$$\partial_t \vec{u}' = (N_{\vec{u}} + L)\vec{u}', \qquad (9)$$

where $N_{\vec{u}}$ is same Jocabian matrix as in Eq. (7). Corresponding eigenvalue problem reads

$$(N_{\vec{u}} + L)\hat{u} = \lambda\hat{u}, \qquad (10)$$

where $\hat{u}$ is the eigenmode corresponding to eigenvalue λ. The stability of the steady base flow is determined by the leading eigenvalues, i.e., those with the largest real parts. For $\Delta t \ll 1$, the solution to the linearized Eq. (9) can be re-formed as

$$\begin{aligned}\vec{u}'(t + \Delta t) &= e^{\Delta t(N_{\vec{u}} + L)}\vec{u}'(t) \\ &\approx \vec{u}'(t) + \Delta t(I - \Delta t L)^{-1}(N_{\vec{u}} + L)\vec{u}'(t). \end{aligned} \qquad (11)$$

Note that the leading eigenvalues of $(N_{\vec{u}} + L)$ are in correspondence with the dominate ones of $e^{\Delta t(N_{\vec{u}} + L)}$ which can be calculated by the Arnoldi method and integrating the linearized Navier-Stokes equations. The Arnoldi algorithm from the ARPACK library [26] is used. The tolerance used in Arnoldi eigenvalue solver is 10^{-5}.

3.2. Validation

In order to validate our algorithms and implementations, we carried out a test case to determine the critical Reynolds number Re_{cr} of the first primary bifurcation of opposed-jet flow with $\theta = 0$. The results are illustrated in Table 1. Three meshes with 4834, 7888 and 11,222 spectral elements are used for the calculation. The elements are clustered near the center and solid walls. A figure depicting the central region of mesh comprising 7888 elements is shown in Fig. 2. In this mesh, element size is $\Delta x = \Delta y = 0.05$ near the center and $\Delta y = 0.05$ in the vertical direction near the solid walls. The base flow and corresponding spectral stability are calculated for $Re = 45$ and $Re = 47$. The largest real parts σ of the eigenvalues are given in Table 1. Then Re_{cr} is determined by linear interpolation. We obtained the converged critical value

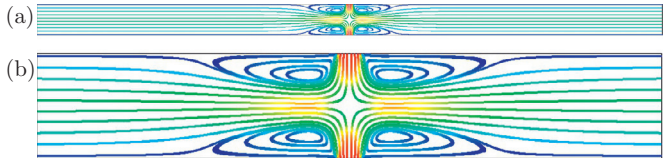

Fig. 3. (a) Streamlines of base flow pattern P_I at $Re = 45.0$. (b) Close-up of the stagnation region. Color code: red (blue) corresponds to largest (lowest) velocity value. (For interpretation of the references to colour in this figure legend, the reader is referred to the web version of this article.)

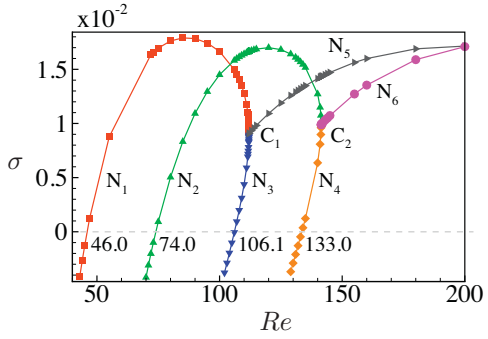

Fig. 4. The real parts σ of leading eigenvalues of base flow pattern P_I as functions of Re.

$Re_{cr} = 46.0$ which is consistent with previous results (the value given in [10] is about 47). Hence, the mesh comprising 7888 elements and 4th-order interpolating polynomials are adequate for giving faithful results of stability analysis and used throughout our study. In addition, we carried out simulations and stability analysis with lengthened computational domain with $L^*/W^* = 15$ at selected Re (including the largest Re we have considered in this study) with $\theta = 0$. The results are consistent with those obtained with $L^*/W^* = 10$. Hence, the shorter one is adequate for giving reliable results and used in the scope of this study. It is noted that direct numerical simulations were conducted at selected Re (including the largest one investigated) and only stable steady solutions were obtained. The results of direct numerical simulation are consistent with those obtained by Newton iteration and linear stability analysis.

4. Results

4.1. Symmetric case

When inlet boundary conditions are symmetric, *i.e.*, $\theta = 0$, the base flow has all the symmetries of the problem. The base flow pattern we name P_I is shown in Fig. 3. The streamlines at $Re = 45.0$ are depicted in Fig. 3(a), and a close-up of the stagnation region is given in Fig. 3(b). There is a stagnation point located half-way between the two inlets. Four recirculation bubbles of equal size can be observed near the stagnation point indicating P_I possesses the D_2 symmetry.

The stable or unstable P_I flow can be obtained using Newton's method. Stability analysis of P_I flow is performed and the real parts σ of leading eigenvalues as functions of Re are depicted in Fig. 4. Six branches $N_1 - N_6$ corresponding to six different eigenmodes are identified, among which four $(N_1 - N_4)$ are steady eigenmodes and two $(N_5 - N_6)$ are unsteady eigenmodes. It is observed from the figure that the six eigenmodes are unstable in certain Re ranges. The base flow pattern P_I may lose stability to new flow patterns.

As shown in Fig. 4, the steady eigenmodes corresponding to $N_1 - N_4$ become unstable sequentially at $Re = 46.0, 74.0, 106.1, 133.0$, respectively. We can observe the

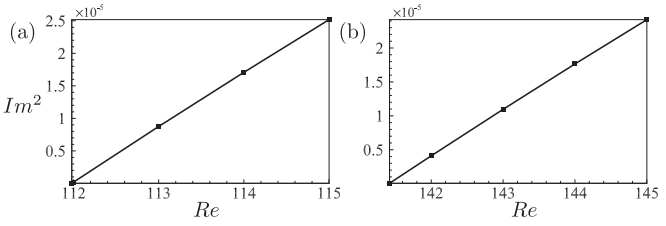

Fig. 5. Scaling law $Im^2 \propto (Re - Re_{cr})$ of imaginary parts Im of eigenvalues in (a) N_5 and (b) N_6 near corresponding critical Re at which collisions happen.

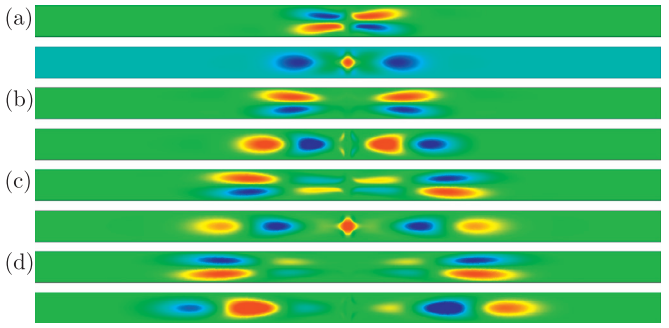

Fig. 6. Contours of horizontal (the upper one) and vertical (the lower one) velocity components of velocity eigenmodes (a) $\vec{\Phi}_1$, (b) $\vec{\Phi}_2$, (c) $\vec{\Phi}_3$ and (d) $\vec{\Phi}_4$ near corresponding critical Re. Color code: red (blue) corresponds to largest (lowest) magnitude. (For interpretation of the references to colour in this figure legend, the reader is referred to the web version of this article.)

branch N_5 (N_6) appears after the collision of N_1 and N_3 (N_2 and N_4) at the collision point C_1 (C_2) which is labeled in the figure. The imaginary part Im of eigenvalue of N_5 (N_6) which represents the oscillating frequency of corresponding eigenmode is found to be proportional to $(Re - Re_{cr})^{0.5}$ near Re_{cr}, where Re_{cr} is the critical Re at which collision C_1 (C_2) happens. In other words, $Im^2 \propto (Re - Re_{cr})$, as depicted in Fig. 5. The emergence of complex eigenvalues after the collisions of real eigenvalues can be explained using model equations as illustrated later.

The velocity eigenmodes $\vec{\Phi}_1 - \vec{\Phi}_4$ corresponding to $N_1 - N_4$ branches near corresponding critical Re are displayed in Fig. 6. Contours of horizontal and vertical velocity components are both presented. It is observed that $\vec{\Phi}_1$ and $\vec{\Phi}_3$ are invariant to spatial reflection K_x about the mid-plane $x = 0$, and $\vec{\Phi}_2$ and $\vec{\Phi}_4$ are invariant to spatial rotation R_π around the center. This observation is important for the construction of model equations.

At $Re = 46.0$, the base flow P_I loses stability through a supercritical pitchfork bifurcation and gives rise to flow pattern P_{II} which is found to be stable throughout the Re range we study using linear stability analysis. The streamlines of P_{II} at $Re = 47.0$ are depicted in Fig. 7(a). P_{II} flow is characterized by the deviation of the stagnation point from the mid-plane $y = 0$ towards the inlet where there are two relatively smaller recirculation bubbles. P_{II} is invariant to spatial reflection K_x about the mid-plane $x = 0$ and possesses the Z_2 symmetry. We remark that P_{II} comprises two solutions which are conjugated by spatial reflection about the mid-plane $y = 0$ and lie on a single group orbit. The distance δ of the stagnation point away from the mid-plane $y = 0$ is an appropriate quantity to quantify the bifurcation from P_I to P_{II}. The bifurcation diagram is depicted in Fig. 7(b). The appearance of flow pattern P_{II} and corresponding critical Re we obtain agree well with previous results [10]. It is noted that P_{II} possesses the same symmetry as the asymmetric steady flow in cross-slot geometry which originates from inertial instability [14]. Similar symmetry-breaking bifurcation was observed in X-junction flow [15] which was due to a lift-up mechanism. It is expected that the same mechanism

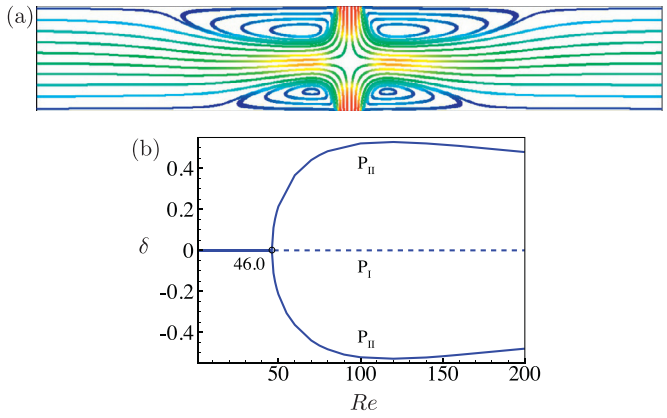

Fig. 7. (a) Streamlines of P_{II} at $Re = 47.0$. (b) Diagram of bifurcation giving rise to P_{II}. Black circle indicates the bifurcation point. Corresponding critical Re is displayed. δ is used as the characteristic quantity. Stable (unstable) patterns are indicated by solid (dashed) branches.

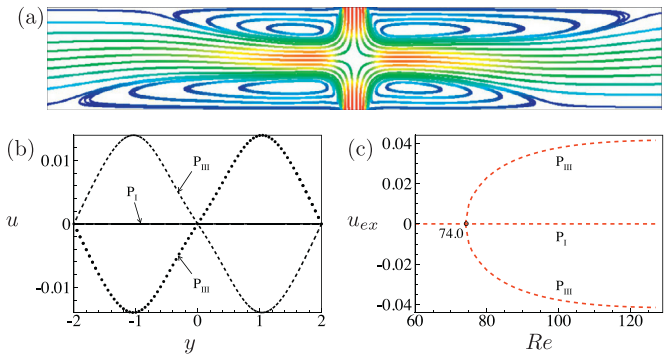

Fig. 8. (a) Streamlines of P_{III} at $Re = 76.0$. (b) Horizontal-velocity profiles of P_I and P_{III} at the cross section $x = 0$ at $Re = 76.0$. (c) Diagram of bifurcation giving rise to P_{III}. Black circle indicates the bifurcation point. Corresponding critical Re is displayed. u_{ex} is used as the characteristic quantity. Dashed branches indicate unstable patterns.

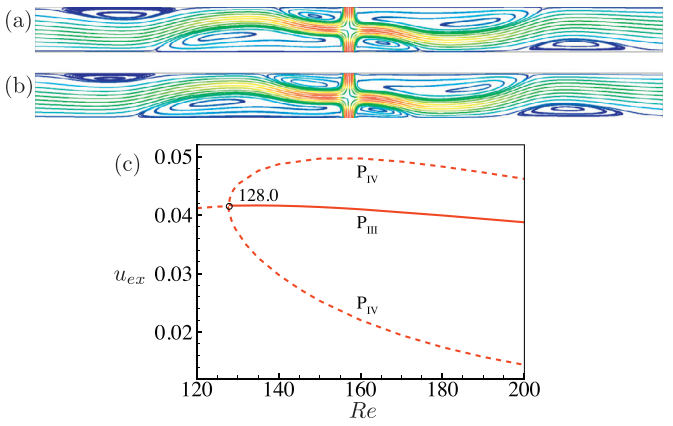

Fig. 9. (a-b) Streamlines of (a) P_{III} and (b) P_{IV} at $Re = 140.0$. (c) Diagram of bifurcation giving rise to P_{IV}. Black circle indicates the bifurcation point. Corresponding critical Re is displayed. u_{ex} is used as the characteristic quantity. Stable (unstable) patterns are indicated by solid (dashed) branches.

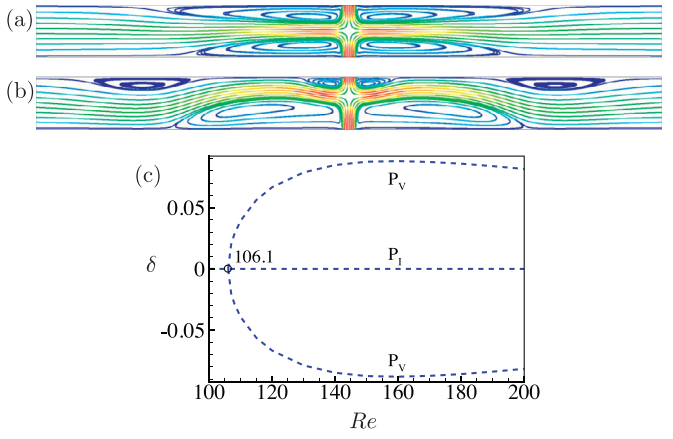

Fig. 10. (a-b) Streamlines of (a) P_V and (b) P_{II} at $Re = 107.0$. (c) Diagram of bifurcation giving rise to P_V. Black circle indicates the bifurcation point. Corresponding critical Re is displayed. δ is used as the characteristic quantity. Dashed branches indicate unstable patterns.

plays an important role in the primary instability of opposed-jet flow considering the similarity of flow structures.

As Re is increased, the base flow P_I gives rise to a new flow pattern P_{III} through a second supercritical pitchfork bifurcation at $Re = 74.0$, as can be identified from Fig. 4. The P_{III} flow is found to be unstable using linear stability analysis, and the streamlines for P_{III} at $Re = 76.0$ are depicted in Fig. 8(a). We also plot the horizontal-velocity profiles of P_I and P_{III} at the cross section $x = 0$ at the same Re in Fig. 8(b). From Fig. 8(a) we observe that P_{III} has two recirculation bubbles of different sizes locating near each inlet. The P_{III} flow is invariant to spatial rotation R_π around the center and possesses the C_2 symmetry. P_{III} also comprises two solutions which are conjugated by spatial reflection about the mid-plane $y = 0$. At this time it is more appropriate to take u_{ex}, the extremum of horizontal velocity u at the cross section $x = 0$ located near the lower inlet, rather than δ as the characteristic quantity to quantify the bifurcation. The bifurcation diagram is depicted in Fig. 8(c).

Taking P_{III} flow as base flow, a secondary pitchfork bifurcation is captured at $Re = 128.0$. After this bifurcation, a new flow pattern P_{IV} appears. The streamlines for P_{III} and P_{IV} at $Re = 140.0$ are depicted in Fig. 9(a) and (b), respectively. It is observed that P_{III} is still invariant to spatial rotation R_π around the center and possesses the C_2 symmetry, while P_{IV} does not possess any nontrivial symmetry. P_{IV} comprises four solutions which are conjugated by spatial reflection about the mid-plane $y = 0$ or $x = 0$, or by spatial rotation R_π around the center. It is found that P_{III} becomes stable after this secondary pitchfork bifurcation by means of linear stability analysis and P_{IV} keeps being unstable throughout the Re range we consider. The bifurcation diagram is depicted in Fig. 9(c) where u_{ex} is used as the characteristic quantity. To the best of our knowledge, stable flow pattern P_{III} has not been reported in previous experimental or numerical studies of opposed-jet flow system. We note that P_{III} possesses the same symmetry as the asymmetric steady flow in cross-slot geometry which originates from elastic instability [12,13]. To our knowledge similar flow pattern originating from inertial instability in cross-slot geometry has not been observed [14].

We come back to the bifurcation of base flow pattern P_I. As Re is further increased, another pitchfork bifurcation occurs at $Re = 106.1$, as can also be identified from Fig. 4. A new flow pattern P_V appears after this bifurcation and is found to be unstable by means of linear stability analysis. The streamlines for P_V flow at $Re = 107.0$ are depicted in Fig. 10(a), and the streamlines for P_{II} flow at the same Re are illustrated in Fig. 10(b) for comparison. We can see that P_V possesses the same symmetry as P_{II}, i.e., the Z_2 symmetry. Just like P_{II}, P_V also comprises two solutions which are conjugated by spatial reflection about the mid-plane $y = 0$. Using δ as the characteristic quantity, the bifurcation diagram is shown in Fig. 10(c).

As revealed from Fig. 4, a fourth pitchfork bifurcation of P_I flow occurs at $Re = 133.0$. Again a new pattern P_{VI} is obtained after this

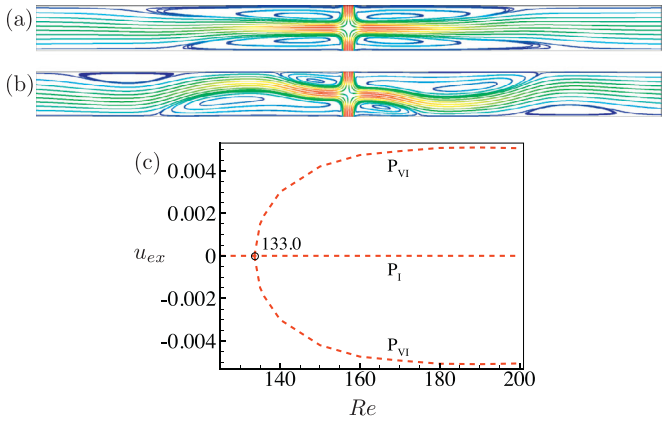

Fig. 11. (a-b) Streamlines of (a) P_{VI} and (b) P_{III} at $Re = 135.0$. (c) Diagram of bifurcation giving rise to P_{VI}. Black circle indicates the bifurcation point. Corresponding critical Re is displayed. u_{ex} is used as the characteristic quantity. Dashed branches indicate unstable patterns.

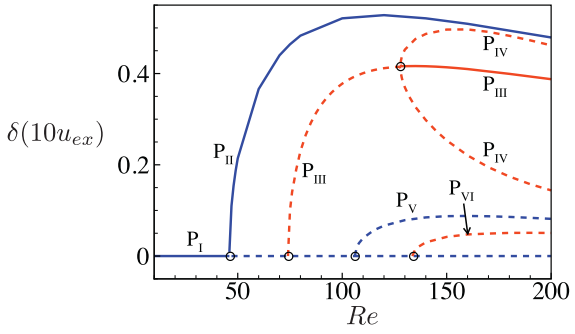

Fig. 12. Bifurcation diagram of opposed-jet flow with $\theta = 0$. Black circles indicate bifurcation points. Blue (red) lines indicate that δ ($10u_{ex}$) is used as the characteristic quantity. Stable (unstable) patterns are indicated by solid (dashed) branches. (For interpretation of the references to colour in this figure legend, the reader is referred to the web version of this article.)

bifurcation and also found to be unstable by means of linear stability analysis. The streamlines of P_{VI} flow at $Re = 135.0$ are depicted in Fig. 11(a), and the streamlines of P_{III} flow at the same Re are shown in Fig. 11(b) for comparison. It is observed that P_{VI} possesses the same symmetry as P_{III}, i.e., the C_2 symmetry. Just like P_{III}, P_{VI} also comprises two solutions which are conjugated by spatial reflection about the mid-plane $y = 0$. Using u_{ex} as the characteristic quantity, we obtain the bifurcation diagram as depicted in Fig. 11(c).

For clarity, a bifurcation diagram summarizing our findings about opposed-jet flow with $\theta = 0$ is shown in Fig. 12. Both δ and $10u_{ex}$ are utilized to illustrate the bifurcation processes. Overall six flow patterns ($P_I - P_{VI}$) are observed, and four of them ($P_{III} - P_{VI}$) are firstly discovered to our knowledge.

4.2. Slightly asymmetric case

When inflow velocities are slightly different, we find that the bifurcation processes are extremely sensitive to this small symmetry-breaking imperfection and much different from those in the symmetric case. Using δ as the characteristic quantity, bifurcation diagram of opposed-jet flow with $\theta = 0.01$ is depicted in Fig. 13. As displayed in the figure, at small Re, there exists only one stable and steady flow pattern AP_I. The streamlines of AP_I at $Re = 20.0$ are depicted in Fig. 14(a). AP_I possesses the Z_2 symmetry as a consequence of asymmetry of inlet boundary conditions. It is observed that, at small Re, the up-down symmetry of AP_I is only slightly broken. AP_I is found to be stable throughout the range of

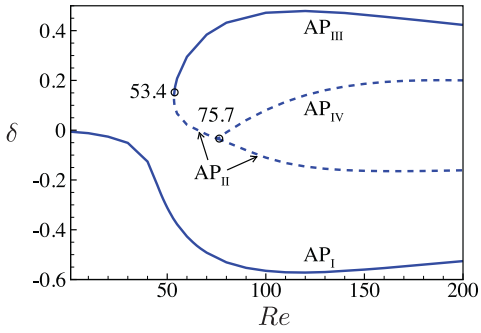

Fig. 13. Bifurcation diagram of opposed-jet flow with $\theta = 0.01$. Black circles indicate bifurcation points. Critical Re for various bifurcations are displayed. δ is used as the characteristic quantity. Stable (unstable) patterns are indicated by solid (dashed) branches.

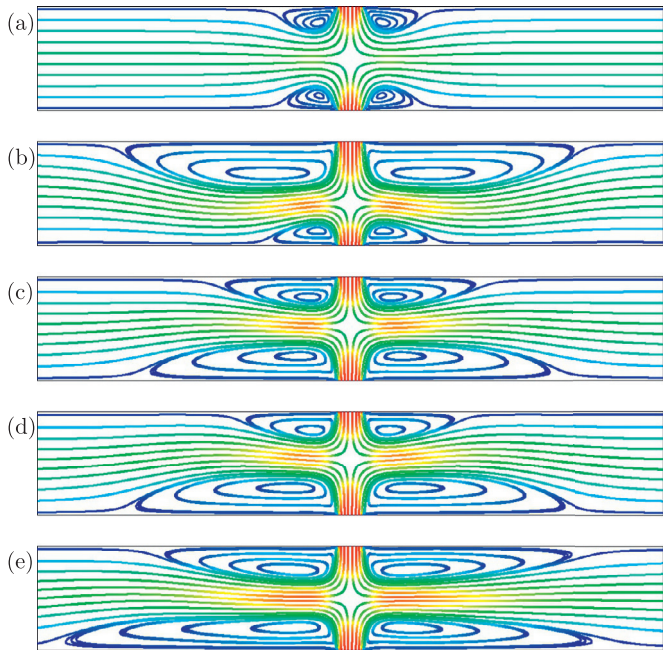

Fig. 14. (a) Streamlines of AP_I at $Re = 20.0$. (b–d) Streamlines of (b) AP_I, (c) AP_{II} and (d) AP_{III} at $Re = 54.0$. (e) Streamlines of AP_{IV} at $Re = 76.0$.

Re we consider by means of linear stability analysis. As Re is increased, a saddle-node bifurcation occurs at $Re = 53.4$ and gives rise to two new flow patterns AP_{II} and AP_{III}. The streamlines of AP_I, AP_{II} and AP_{III} at $Re = 54.0$ are shown in Fig. 14(b)–(d), respectively. It is observed that AP_{II} and AP_{III} possess the same symmetry as AP_I, i.e., the Z_2 symmetry. By means of linear stability analysis it is found that AP_{II} is unstable whereas AP_{III} is stable. Actually, up-down asymmetry forced by asymmetric inlet boundary conditions induces the first primary pitchfork bifurcation in the symmetric case to be imperfect. As Re is further increased, AP_{II} gives rise to a new flow pattern AP_{IV} through a pitchfork bifurcation at $Re = 75.7$. The streamlines of AP_{IV} at $Re = 76.0$ are depicted in Fig. 14(e). It is observed that AP_{IV} does not possess any nontrivial symmetry. AP_{IV} comprises two solutions which are conjugated by spatial reflection about the mid-plane $x = 0$. Corresponding solution branches overlap in Fig. 13. Linear stability analysis demonstrates that AP_{IV} is unstable.

Bifurcation analysis of opposed-jet flow with $\theta = 0.02$ is also performed and the results are similar to those with $\theta = 0.01$. We remark that bifurcations with $\theta = 0.02$ occur at slightly larger Re than their counterparts with $\theta = 0.01$.

4.3. Model equations

When $\theta = 0$, the governing Eq. (1), boundary conditions and the base flow pattern P_I are invariant to spatial reflection $K_x(x, y) \to (-x, y)$ and spatial rotation $R_\pi(x, y) \to (-x, -y)$; hence, bifurcations occur in the presence of D_2 symmetry. Near the threshold of mode-interaction of eigenmodes $\vec{\Phi}_1$ and $\vec{\Phi}_2$ of the base flow pattern P_I the dynamics of opposed-jet flow can be reduced to a center manifold (a_1, a_2) where a_i give the amplitudes for the eigenmodes $\vec{\Phi}_i$

$$\vec{\Phi}(t; x, y) = a_1(t)\vec{\Phi}_1(x, y) + a_2(t)\vec{\Phi}_2(x, y) + (\textit{remaining stable modes}). \tag{12}$$

The symmetries of eigenmodes $\vec{\Phi}_1$ and $\vec{\Phi}_2$ determine how the D_2 symmetry acts on the center manifold variables [16]; we have

$$K_x(a_1, a_2) = (a_1, -a_2),$$
$$R_\pi(a_1, a_2) = (-a_1, a_2). \tag{13}$$

The equations for a_1 and a_2 will be symmetric with respect to this action which implies they have the form

$$\frac{da_1}{dt} = g_1(a_1^2, a_2^2)a_1,$$
$$\frac{da_2}{dt} = g_2(a_1^2, a_2^2)a_2. \tag{14}$$

Expanding Eq. (14) to third order we have

$$\frac{da_1}{dt} = ra_1 + Aa_1^3 + Ba_1a_2^2,$$
$$\frac{da_2}{dt} = ra_2 + Ca_2^3 + Da_1^2a_2, \tag{15}$$

where r is the bifurcation parameter and plays the role of Re in opposed-jet flow system. Coefficients in Eq. (15) are chosen such that $D < A < 0$ and $B < C < 0$, guaranteeing that "pure mode solutions" $(a_1, 0)$ and $(0, a_2)$ bifurcate from the base solution (0, 0) supercritically at $r = 0$ and are stable. When a_1 and a_2 are scaled appropriately, Eq. (15) can be rewritten as

$$\frac{da_1}{dt} = ra_1 - a_1^3 + \bar{B}a_1a_2^2,$$
$$\frac{da_2}{dt} = ra_2 - a_2^3 + \bar{D}a_1^2a_2. \tag{16}$$

It is noted that in opposed-jet flow system eigenmodes $\vec{\Phi}_1$ and $\vec{\Phi}_2$ become unstable at different Re and when $\theta \neq 0$, the up-down symmetry is broken and the system is equivariant to only the spatial reflection K_x about mid-plane $x = 0$. Thus, we unfold Eq. (16) as

$$\frac{da_1}{dt} = ra_1 - a_1^3 - 2a_1a_2^2 - h,$$
$$\frac{da_2}{dt} = \bar{r}a_2 - a_2^3 - 2a_1^2a_2, \tag{17}$$

where coefficients are appropriately chosen ($\bar{B} = \bar{D} = -2$ and $\bar{r} = r - 1$). h measures the extent to which the system is asymmetric and plays the role of θ in opposed-jet flow system. When $h \neq 0$, model Eq. (17) are invariant to the action $K_x(a_1, a_2) = (a_1, -a_2)$ and the equation for a_1 is inhomogeneous ($(0, a_2)$ is no longer a stationary solution).

Bifurcation diagrams of model Eq. (17) with $h = 0$ and 0.1 are depicted in Fig. 15(a) and (b), respectively. Blue (red) lines indicate that a_1 (a_2) is used as the characteristic quantity. When $h = 0$, the base solution (0, 0) gives rise to "pure mode solutions" $(a_1, 0)$ and $(0, a_2)$ through two primary bifurcations sequentially. Corresponding critical r are 0.0 and 1.0, respectively. $(a_1, 0)$ is stable and $(0, a_2)$ is unstable. As r is increased, solution $(0, a_2)$ gives rise to a "mixed mode solution" (a_1, a_2) through a secondary pitchfork bifurcation at $r = 2.0$ and becomes stable. It is noted that, with a_2 as the characteristic quantity, the unstable branch coming off at r = 2.0 is actually an overlapping of two solution branches which are conjugate with each other under the action R_π and possess the same a_2 values. When $h = 0.1$ and r is small, only one solution in the form of $(a_1, 0)$ exists and is stable. As r is increased, a saddle-noddle bifurcation occurs at $r = 0.4$ and two solutions in the form of $(a_1, 0)$ appear, among which the unstable one goes through a pitchfork bifurcation at $r = 1.0$ and gives rise to new solutions $(a_1, \pm a_2)$ which possess the same a_1 values. Comparing Fig. 15 with Figs. 12 and 13, it is observed that the nonlinear behaviors of model Eq. (17) with $h = 0$ and $h = 0.1$ are similar with those of opposed-jet flow with $\theta = 0$ and $\theta = 0.01$, respectively (it is noted that only the first two eigenmodes are taken into account in the model equations). The critical Re at which eigenmodes $\vec{\Phi}_1$ and $\vec{\Phi}_2$ of base flow pattern P_I become unstable are 46.0 and 74.0, respectively. Although the difference between these two critical Re is relatively large, model equations constructed based on center manifold theorem and symmetry consideration with appropriate coefficients can capture the nonlinear behaviors of opposed-jet flow and the effects of forced up-down asymmetry qualitatively.

As displayed in Fig. 15, the first primary pitchfork bifurcation in the symmetric case becomes imperfect when $h = 0.1$. When we set $a_2 = 0$ and fix r in Eq. (17), solution $(a_1, 0)$ is a function of h. As displayed in Fig. 16(a), at selected r, a_1 changes smoothly as h varies. As r increases and remains being negative, the rate of change of a_1 at $h = 0$ increases and will diverge when $r = 0$. When $r > 0$, as h varies around $h = 0$ a hysteresis loop is observed, as displayed in Fig. 16(b) for $r = 1$. Similar phenomena can indeed happen in opposed-jet flow system. When $Re = 45.0$, as displayed in Fig. 16(c), δ changes smoothly with θ and no hysteresis loop is present. When Re is increased to 60.0, as displayed in Fig. 16(d), we obtain a hysteresis loop as θ varies around $\theta = 0$. It's another manifestation of the fact that the first primary pitchfork bifurcation becomes imperfect when asymmetry is introduced. It is noted that the appearance of hysteresis loop here is analogous with the experimental results of Ciani et al. [11].

Now we try to understand using model equations the emergence of complex eigenvalues after collisions of real eigenvalues in symmetric opposed-jet flow system as displayed in Fig. 4. Supposing that the dynamics of opposed-jet flow can be reduced to a center manifold (a_1, a_2, a_3, a_4) near the threshold of mode-interaction of eigenmodes $\vec{\Phi}_1 - \vec{\Phi}_4$ where a_i give the amplitudes for the eigenmodes $\vec{\Phi}_i$

$$\vec{\Phi}(t; x, y) = a_1(t)\vec{\Phi}_1(x, y) + a_2(t)\vec{\Phi}_2(x, y) + a_3(t)\vec{\Phi}_3(x, y) + a_4(t)\vec{\Phi}_4(x, y) + (\textit{remaining stable modes}). \tag{18}$$

Equations for $a_1 - a_4$ are symmetric with respect to action (13) and they have the form

$$\frac{da_1}{dt} = g_{11}(a_1^2, a_2^2, a_3^2, a_4^2)a_1 + g_{12}(a_1^2, a_2^2, a_3^2, a_4^2)a_3,$$
$$\frac{da_2}{dt} = g_{21}(a_1^2, a_2^2, a_3^2, a_4^2)a_2 + g_{22}(a_1^2, a_2^2, a_3^2, a_4^2)a_4,$$
$$\frac{da_3}{dt} = g_{31}(a_1^2, a_2^2, a_3^2, a_4^2)a_3 + g_{32}(a_1^2, a_2^2, a_3^2, a_4^2)a_1,$$
$$\frac{da_4}{dt} = g_{41}(a_1^2, a_2^2, a_3^2, a_4^2)a_4 + g_{42}(a_1^2, a_2^2, a_3^2, a_4^2)a_2. \tag{19}$$

Unfolding Eq. (19) and taking only the linear part we have

$$\frac{d}{dt}\begin{pmatrix} a_1 \\ a_3 \\ a_2 \\ a_4 \end{pmatrix} = \begin{pmatrix} S_1 & \\ & S_2 \end{pmatrix}\begin{pmatrix} a_1 \\ a_3 \\ a_2 \\ a_4 \end{pmatrix}, \tag{20}$$

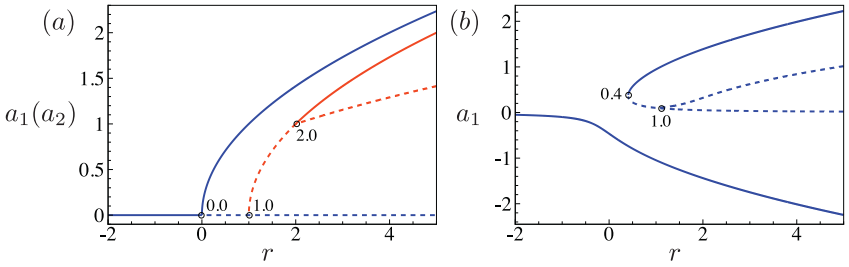

Fig. 15. Bifurcation diagrams of model Eq. (17) with (a) $h = 0$ and (b) $h = 0.1$. Black circles indicate bifurcation points. Critical r for various bifurcations are displayed. Blue (red) lines indicate that a_1 (a_2) is used as the characteristic quantity. Stable (unstable) solutions are indicated by solid (dashed) branches. (For interpretation of the references to colour in this figure legend, the reader is referred to the web version of this article.)

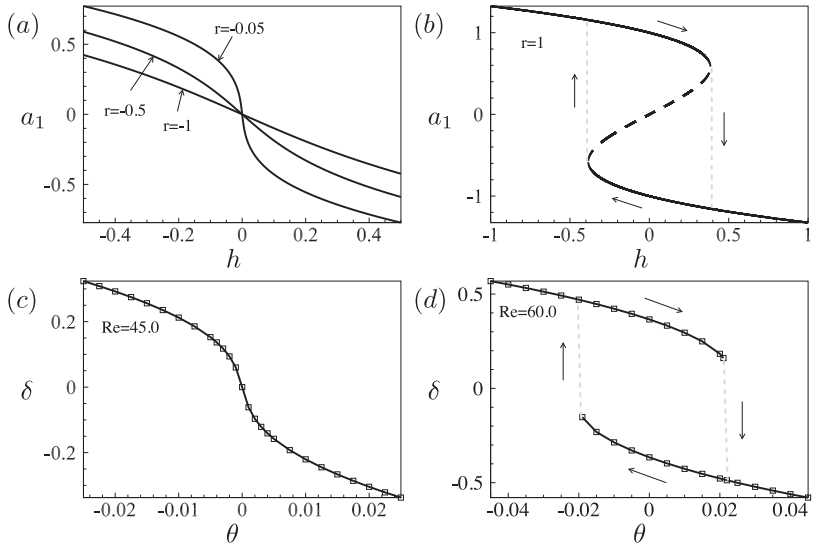

Fig. 16. (a-b) Solution (a_1, 0) to model Eq. (17) as a function of h with r fixed at (a) −1, −0.5, −0.05 and (b) 1. (c-d) δ of opposed-jet flow as a function of θ for (c) $Re = 45.0$ and (d) $Re = 60.0$.

where

$$S_1 = \begin{pmatrix} s_{11} & s_{12} \\ s_{21} & s_{22} \end{pmatrix}, \quad S_2 = \begin{pmatrix} s_{33} & s_{34} \\ s_{43} & s_{44} \end{pmatrix}. \tag{21}$$

s_{ij} are functions of the bifurcation parameter r. The characteristic equation of matrix S_1 is $\lambda^2 - T\lambda + D = 0$, where $T = s_{11} + s_{22}$ and $D = s_{11}s_{22} - s_{21}s_{12}$ are the trace and determinant of S_1. When $\Delta \equiv T^2 - 4D > 0$, eigenvalues of S_1 are real, whereas when $\Delta < 0$, eigenvalues are complex. Assume that S_1 has a real eigenvalue λ_1 of multiplicity two at $r = r_1$ which indicates that N_1 and N_3 branches in Fig. 4 collide. Thus, we have $T(r_1) = 2\lambda_1$ and $D(r_1) = \lambda_1^2$. With $dr = r - r_1 \sim o(1)$, using Taylor expansion we have

$$\Delta = 4\left(\lambda_1 \frac{dT}{dr} - \frac{dD}{dr}\right)\Big|_{r=r_1} dr + O(dr^2). \tag{22}$$

If $\left(\lambda_1 \frac{dT}{dr} - \frac{dD}{dr}\right)|_{r=r_1} \neq 0$, it can be obtained that $\Delta \sim dr$. This approximately linear relationship between Δ and dr near $r = r_1$ implies that the sign of Δ changes when r is increased beyond r_1. This is consistent with the observation that complex eigenvalue pair emerges after collision of two real eigenvalue branches in symmetric opposed-jet flow system. Based on the results of linear stability analysis of the Navier–Stokes equations, we have $\Delta > 0$ ($\Delta < 0$) for $r < r_1$ ($r > r_1$). What might need clarification is that our simplified analysis cannot determine the explicit dependence of T or D with r. Note also that the imaginary part Im of the new complex eigenvalue pair is proportional to $\sqrt{|\Delta|}$. This implies that $Im^2 \propto dr$ when $dr \sim o(1)$, which is consistent with numerical results based on hydrodynamic equations as displayed in Fig. 5. The emergence of complex eigenvalue pair after the collision of N_2 and N_4 can be explained similarly. Above arguments imply that the emergence of complex eigenvalues originates from the fact that eigenmodes of the two eigenvalue branches which collide with each other possess the same symmetry. It is noted that eigenmodes $\vec{\Phi}_1$ and $\vec{\Phi}_2$ possess different symmetries and complex eigenvalue pair does not appear when corresponding eigenvalue branches N_1 and N_2 collide in Fig. 4. This is consistent with our explanation about the emergence of complex eigenvalues.

5. Conclusion

To predict various flow patterns in opposed-jet flow system is of great practical importance and theoretical significance. In this study, numerical bifurcation analysis is performed for laminar isothermal planar opposed-jet flow with geometric parameter $\alpha = 0.25$. Cases with symmetric and slightly asymmetric inlet boundary conditions are both investigated. Rich flow patterns are observed.

In the symmetric case, within the range of $Re \leq 200.0$, multiple symmetry-breaking bifurcations are observed. Six flow patterns are identified, i.e., $P_I - P_{VI}$, among which $P_{III} - P_{VI}$ are firstly discovered. P_I possesses the D_2 symmetry, P_{II} and P_V possess the Z_2 symmetry, P_{III} and P_{VI} possess the C_2 symmetry, while P_{IV} does not possess any nontrivial symmetry. In the range of Re we consider, linear stability analysis shows that, among bifurcated flow patterns, P_{II} is stable and $P_{IV} - P_{VI}$ are unstable. P_{III} becomes stable after a secondary pitchfork bifurcation.

When inlet boundary conditions are slightly asymmetric, it is found that bifurcation processes are extremely sensitive to this small symmetry-breaking imperfection and much different from those in the symmetric case. Four flow patterns, i.e., $AP_I - AP_{IV}$, are observed. $AP_I - AP_{III}$ possess the Z_2 symmetry, while AP_{IV} does not possess any nontrivial symmetry. Stability analysis demonstrates that AP_I and AP_{III} are stable, while AP_{II} and AP_{IV} are unstable in the range of Re we consider.

Model equations are constructed by symmetry consideration and used to explain numerical results based on hydrodynamic Eq. (1). With appropriate coefficients, model Eq. (17) can qualitatively capture nonlinear behaviors of opposed-jet flow and the effects of forced up-down asymmetry. It is observed that δ of opposed-jet flow varies smoothly with θ at small Re and a hysteresis loop appears when Re is large enough. This is consistent with the results of model equations. It is another manifestation of the fact that the first primary pitchfork bifurcation becomes imperfect when asymmetry is introduced. In symmetric opposed-jet flow system, the real parts σ of leading eigenvalues of base flow pattern P_I vary with Re and complex eigenvalues emerge after collisions of real eigenvalues. The emergence of complex eigenvalues is explained using model equations as well.

Acknowledgments

This work was supported by National Natural Science Foundation of China (Grant Nos. 11232011, 11402262, 11572314, 11502137), China Postdoctral Science Foundation funded project (Grant No. 2014M561833), the Fundamental Research Funds for the Central Universities and the 111 Project of China under Grant No. B07033.

References

[1] Wood P, Hrymak A, Yeo R, Johnson D, Tyagi A. Experimental and computational studies of the fluid mechanics in an opposed jet mixing head. Phys Fluids A 1991;3(5):1362–8.
[2] Sarigiannis D, Peck JD, Kioseoglou G, Petrou A, Mountziaris T. Characterization of vapor-phase-grown znse nanoparticles. Appl Phys Lett 2002;80:4024.
[3] Tamir A. Impinging-stream reactors: fundamentals and applications. Elsevier; 1994.
[4] Wu Y. Impinging streams: fundamentals, properties and applications. Elsevier; 2007.
[5] Linan A. The asymptotic structure of counterflow diffusion flames for large activation energies. Acta Astronaut 1974;1(7):1007–39.
[6] Fotache C, Kreutz T, Law C. Ignition of counterflowing methane versus heated air under reduced and elevated pressures. Combustion Flame 1997;108(4):442–70.
[7] Rolon J, Veynante D, Martin J, Durst F. Counter jet stagnation flows. Exp Fluids 1991;11(5):313–24.
[8] Denshchikov V, Kondrat'ev V, Romashov A. Interaction between two opposed jets. Fluid Dyn 1978;13(6):924–6.
[9] Denshchikov V, Kondrat'ev V, Romashov A, Chubarov V. Auto-oscillations of planar colliding jets. Fluid Dyn 1983;18(3):460–2.
[10] Pawlowski R, Salinger A, Shadid J, Mountziaris T. Bifurcation and stability analysis of laminar isothermal counterflowing jets. J Fluid Mech 2006;551:117.
[11] Ciani A, Kreutner W, Frouzakis C, Lust K, Coppola G, Boulouchos K. An experimental and numerical study of the structure and stability of laminar opposed–jet flows. Comput Fluids 2010;39:114.
[12] Arratia PE, Thomas C, Diorio J, Gollub JP. Elastic instabilities of polymer solutions in cross-channel flow. Phys Rev Lett 2006;96(14):144502.
[13] Poole R, Alves M, Oliveira P. Purely elastic flow asymmetries. Phys Rev Lett 2007;99(16):164503.
[14] Poole R, Rocha G, Oliveira P. A symmetry-breaking inertial bifurcation in a cross-slot flow. Comput Fluids 2014;93:91–9.
[15] Lashgari I, Tammisola O, Citro V, Juniper MP, Brandt L. The planar X-junction flow: stability analysis and control. J Fluid Mech 2014;753:1–28.
[16] Crawford JD, Knobloch E. Symmetry and symmetry-breaking bifurcations in fluid dynamics. Annu Rev Fluid Mech 1991;23(1):341–87.
[17] Hoyle RB. Pattern formation: an introduction to methods. Cambridge University Press; 2006.
[18] Golubitsky M, Stewart I, Schaeffer D. Singularities and groups in bifurcation theory. New York: Springer-verlag; 1988.
[19] Sherwin SJ, Ainsworth M. Unsteady navier–stokes solvers using hybrid spectral/hp element methods. Appl Numer Math 2000;33:357.
[20] Karniadakis G, Sherwin S. Spectral/hp element methods for computational fluid dynamics. Oxford University Press; 2005.
[21] Karniadakis GE, Israeli M, Orszag SA. High-order splitting methods for the incompressible Navier–Stokes equations. J Comput Phys 1991;97(2):414–43.
[22] Knoll DA, Keyes DE. Jacobian-free Newton-Krylov methods: a survey of approaches and applications. J Comput Phys 2004;193:357.
[23] Tuckerman L, Barkley D. Bifurcation analysis for timesteppers. In: Doedel E, Tuckerman L, editors. Numerical methods for bifurcation problems and large-scale dynamical systems, vol. 119; 2000. p. 453.
[24] Eisenstat SC, Walker HF. Globally convergent inexact newton methods. SIAM J Optim 1994;4(2):393–422.
[25] Pernice M, Walker HF. Nitsol: a Newton iterative solver for nonlinear systems. SIAM J Sci Comput 1998;19(1):302–18.
[26] Lehoucq RB, Sorensen DC, Yang C. ARPACK users' guide: solution of large-scale eigenvalue problems with implicitly restarted Arnoldi methods, vol. 6. Siam; 1998.